




 Cite this: *RSC Adv.*, 2017, 7, 38179

A family of lanthanide compounds based on nitronyl nitroxide radicals: synthesis, structure, magnetic and fluorescence properties†

 Xue-Hui Lv,^a Shuai-Liang Yang,^a Yuan-Xia Li,^a Chen-Xi Zhang ^{*ab}
and Qing-Lun Wang ^{*bc}

A series of lanthanide nitronyl nitroxide radical compounds, $[\text{Ln}(\text{hfac})_3(\text{NITPh-}p\text{-N}(\text{CH}_3)_2)_2] \cdot x\text{C}_7\text{H}_{16}$ (Ln = La (1), Eu (2), Gd (3), Tb (4), Dy (5), Er (6), hfac = hexafluoroacetylacetonate; NITPh-*p*-N(CH₃)₂ = 4'-dimethylamino-phenyl-4,4,5,5-tetramethylimidazoline-1-oxyl-3-oxide, $x = 2/3$ for complexes 1, 2, 3 and 6, and 0 for 4 and 5), have been synthesized and structurally characterized. X-Ray crystallographic analyses show that the structures of the six compounds are similar and all consist of isolated molecules, in which central Ln(III) ions are coordinated to six oxygen atoms from three hexafluoroacetylacetonate ligands and two oxygen atoms from nitronyl nitroxide radicals. Variable-temperature magnetic susceptibility studies reveal ferromagnetic interactions between the Gd(III) ion and nitronyl nitroxide radical in complex 3. Ac magnetic susceptibility measurements of complexes 4 and 5 exhibit frequency-dependent out-of-phase signals, indicating single-molecule magnet (SMM) behavior.

Received 22nd May 2017

Accepted 27th July 2017

DOI: 10.1039/c7ra05764d

rsc.li/rsc-advances

Introduction

The study of molecular nanomagnets showing slow relaxation of the magnetization is one of the key topics in the field of molecular magnetism.¹ Molecular nanomagnets mainly include single-molecule magnets (SMMs)² and single-chain magnets (SCMs).³ SMMs and SCMs not only permit the observation of fascinating quantum phenomena but also are investigated as potential candidates for future high-density data storage materials. SMMs and SCMs exhibit slow relaxation of magnetization due to a large ground-state spin quantum number (S), a significant uniaxial magneto-anisotropy ($D < 0$), and a good magnetic isolation of the molecule.

Lanthanide (Ln) ions have become attractive candidates for constructing new SMMs and SCMs because most of them have significant magnetic anisotropy arising from the large unquenched orbital angular momentum. As a result, many lanthanide complexes with SMM behavior have become attractive synthetic targets for chemists.⁴

The stability of the radicals like nitronyl nitroxide at a relatively high temperature has made them potential systems in molecular magnetism.⁵ Recently, nitronyl nitroxides and lanthanide ions were successfully synthesized to obtain the SMMs and SCMs,⁶ especially heavy lanthanide ions such as terbium(III) and dysprosium(III).⁷ Since the terbium(III) and dysprosium(III) ions have large anisotropies,⁸ synthesis and characterization of terbium(III) and dysprosium(III) with the nitronyl nitroxide have already set the fashion in the field of molecular magnetism.^{9–11} For example, complex $[\text{Tb}_3(\text{hfac})_9(\text{NIT-2thien})_3]_n$ showed the coexistence of spin canting, metamagnetism, spin dynamic relaxation and magnetic ordering.⁹ $[\text{Dy}(\text{hfac})_3(\text{PyNO})_2]$ shows a remarkable SMM behavior with complex hysteresis at 1.4 K.¹⁰ One-dimensional chain complex $[\text{Tb}(\text{hfac})_3(\text{NITPhSCH}_3)]_n$ is the first example of radical–metal SMM units in the construction of an SCM system.¹¹

It is very interesting to develop new nitronyl nitroxide complexes and better understand the nature of 2p–4f magnetic interaction. In this paper, by using a new nitronyl nitroxide radical NITPh-*p*-N(CH₃)₂ and lanthanide ions, a series of novel 2p–4f complexes were synthesized. Herein we report a detailed study of the magnetic properties of a novel family of 2p–4f complexes: $[\text{Ln}(\text{hfac})_3(\text{NITPh-}p\text{-N}(\text{CH}_3)_2)_2] \cdot x\text{C}_7\text{H}_{16}$, (Ln = La (1), Eu (2), Gd (3), Tb (4), Dy (5) and Er (6), $x = 2/3$ for complexes 1, 2, 3 and 6 while 0 for 4 and 5). Complexes 4 and 5 present slow relaxation of the magnetization at low temperature, suggesting single-molecule magnet behavior.

^aCollege of Chemical Engineering and Materials Science, Tianjin University of Science and Technology, Tianjin 300457, P. R. China. E-mail: zcx@tust.edu.cn

^bKey Laboratory of Advanced Energy Materials Chemistry (Ministry of Education), Nankai University, Tianjin 300071, P. R. China. E-mail: wangql@nankai.edu.cn

^cCollege of Chemistry, Nankai University, Tianjin 300071, P. R. China

† Electronic supplementary information (ESI) available: Appendix A. CCDC 1063970 (1), 1063969 (2), 1063967 (3), 1063968 (4), 957789 (5), 1063966 (6) contain the supplementary crystallographic data for this paper. For ESI and crystallographic data in CIF or other electronic format see DOI: 10.1039/c7ra05764d



Experimental section

Materials and physical measurements

All reagents and solvents were purchased from commercial sources and used without purification. Ln(hfac)₃·2H₂O (La, Eu, Gd, Tb, Dy, Er)¹² and NITPh-*p*-N(CH₃)₂ (ref. 13) were synthesized according to the reported methods.

Infrared spectra were recorded on a Perkin-Elmer Spectrum One spectrometer using KBr pellets in the region 4000–400 cm⁻¹. Elemental analyses for C, H, and N were measured by a Perkin-Elmer 240 elemental analyzer. The X-ray powder diffraction patterns (PXRD) have been recorded on a Shimadzu LabX XRD-6100 diffractometer, operated at 40.0 kV and 30.0 mA, using a Cu target tube and graphite monochromator. The intensity data were recorded by continuous scan in 2θ/θ mode from 5° to 50° with a step size of 0.02° and a scan speed of 5° min⁻¹. The thermogravimetry-differential thermal analysis (TG-DTA) was studied by SDT-Q600 at a heating rate of 20 C min⁻¹ in nitrogen atmosphere, and nitrogen gas of high purity (>99.999%) with a flow rate of 100 mL min⁻¹ was used as carrier gas. The sample was heated from ambient temperature to 600 °C. Luminescence properties were recorded on an F-4500 FL spectrophotometer with a xenon arc lamp as the light source. The magnetic measurements were carried out with a MPMS XL-7 SQUID magnetometer. The samples are embedded in grease to avoid preferential orientation of the micro-crystallites. Diamagnetic corrections were made with Pascal's constants for all of the constituent atoms.¹⁴

Synthesis procedures

Syntheses of [La(hfac)₃(NITPh-*p*-N(CH₃)₂)₂]₃·2/3C₇H₁₆ (1). 41 mg (0.05 mmol) of La(hfac)₃·2H₂O was dissolved in 15 mL of boiling heptanes for azeotropically removing hydration water of molecules. Then the solution was cooled to 70 °C, a solution of NITPh-*p*-N(CH₃)₂ (30 mg, 0.1 mmol) in 3 mL CH₂Cl₂ was added. The resulting blue solution was stirred for 15 min and cooled down to room temperature. The filtrate was allowed standing for 5 days, and dark green crystals suitable for X-ray diffraction were obtained. Anal. calc. for C₄₅H₇₀F₁₈LaN₆O₁₀ (yield: 42%): C 40.44%, H 5.24%, N 6.29%. Found: C 40.23%, H 5.18%, N 6.19%. IR (KBr) ν/cm⁻¹: 1650 (vs), 1606 (w) 1552 (w), 1378 (w), 1359 (w), 1256 (vs), 1200 (vs), 1098 (w), 734 (w), 665 (w).

Syntheses of [Eu(hfac)₃(NITPh-*p*-N(CH₃)₂)₂]₃·2/3C₇H₁₆ (2). Compound 2 was obtained in a similar manner for 1 except that Eu(hfac)₃·2H₂O was used instead of La(hfac)₃·2H₂O. Anal. calc. for C₄₅H₇₀F₁₈EuN₆O₁₀ (yield: 45%): C 40.05%, H 5.19%, N 6.23%. Found: C 39.94%, H 5.04%, N 6.14%. IR (KBr) ν/cm⁻¹: 1653 (vs), 1611 (w) 1553 (w), 1373 (w), 1347 (w), 1253 (vs), 1202 (vs), 1095 (w), 738 (w), 622 (w).

Syntheses of [Gd(hfac)₃(NITPh-*p*-N(CH₃)₂)₂]₃·2/3C₇H₁₆ (3). Compound 3 was obtained in a similar manner for complex 1 except that Gd(hfac)₃·2H₂O was used instead of La(hfac)₃·2H₂O. Anal. calc. for C₄₅H₇₀F₁₈GdN₆O₁₀ (yield: 43%): C 39.89%, H 5.17%, N 6.20%. Found: C 39.96%, H 5.20%, N 6.25%. IR (KBr) ν/cm⁻¹: 1609 (vs), 1556 (w), 1375 (w), 1347 (w), 1255 (vs), 1198 (vs), 1095 (w), 791 (w), 664 (w).

Syntheses of [Tb(hfac)₃(NITPh-*p*-N(CH₃)₂)₂]₃ (4). Compound 4 was obtained in a similar manner for complex 1 except that Tb(hfac)₃·2H₂O was used instead of La(hfac)₃·2H₂O. Anal. calc. for C₄₅H₇₀F₁₈TbN₆O₁₀ (yield: 40%): C 39.84%, H 5.16%, N 6.20%. Found: C 39.68%, H 5.02%, N 6.04%. IR (KBr) ν/cm⁻¹: 1609 (vs), 1609 (w) 1553 (w), 1375 (w), 1356 (w), 1254 (vs), 1198 (vs), 1097 (w), 736 (w), 624 (w).

Syntheses of [Dy(hfac)₃(NITPh-*p*-N(CH₃)₂)₂]₃ (5). Compound 5 was obtained in a similar manner for complex 1 except that Dy(hfac)₃·2H₂O was used instead of La(hfac)₃·2H₂O. Anal. calc. for C₄₅H₇₀F₁₈DyN₆O₁₀ (yield: 38%): C 39.74%, H 5.15%, N 6.18%. Found: C 39.66%, H 5.07%, N 6.03%. IR (KBr) ν/cm⁻¹: 1655 (vs), 1528 (w), 1387 (w), 1352 (w), 1255 (vs), 1199 (vs), 1095 (w), 795 (w), 661 (w).

Syntheses of [Er(hfac)₃(NITPh-*p*-N(CH₃)₂)₂]₃·2/3C₇H₁₆ (6). Compound 6 was obtained in a similar manner for complex 1 except that Er(hfac)₃·2H₂O was used instead of La(hfac)₃·2H₂O. Anal. calc. for C₄₅H₇₀F₁₈ErN₆O₁₀ (yield: 36%): C 39.60%, H 5.13%, N 6.16%. Found: C 39.43%, H 5.01%, N 6.14%. IR (KBr) ν/cm⁻¹: 1610 (vs), 1558 (w) 1531 (w), 1379 (w), 1346 (w), 1256 (vs), 1204 (vs), 1103 (w), 739 (w), 623 (w).

Crystal structure determination

Crystals of complexes 1–6 were mounted on glass fibers. Determination of the unit cell and data collection were performed with Mo-K_α radiation (λ = 0.71073 Å) on a Bruker SMART 1000 diffractometer and equipped with a CCD camera. The ω-φ scan technique was employed. The structures were solved primarily by direct method and second by Fourier difference techniques and refined by the full-matrix least-squares method. The computations were performed with the SHELXL-97 program.¹⁵ Non-hydrogen atoms were refined anisotropically. The hydrogen atoms were set in calculated positions and refined as riding atoms with a common fixed isotropic thermal parameter. A summary of the crystallographic data and structure refinement is given in Table 1. Selected bond distances and angles for 1–6 are listed in Table S1 (see ESI†). CCDC 1063970 (1), 1063969 (2), 1063967 (3), 1063968 (4), 957789 (5), 1063966 (6), contain the supplementary crystallographic data for this paper.†

Results and discussion

Crystal structure

Complexes 1, 2, 3, 4 and 6 crystallize in the monoclinic space group C2/c, while 5 crystallizes in the monoclinic space group P2₁/n. There are solvent molecules in complexes 1, 2, 3 and 6, while no solvent molecule in complexes 4 and 5. Crystal data and details of structural determination refinement are summarized in Table 1, and selected bond distances and angles for complexes 1–6 are listed in Table S1 in the ESI.†

The structural analyses show that complexes 1–6 are very similar; hence, only the crystal structure of complex 3 is described here. Complex 3 consists of the [Gd(hfac)₃(NITPh-*p*-N(CH₃)₂)₂]₃ unit and solvent molecule of C₇H₁₆. The structure of [Gd(hfac)₃(NITPh-*p*-N(CH₃)₂)₂]₃ unit in complex 3 is shown in



Table 1 Crystal data and structure refinements for complexes 1–6

Compound	1	2	3	4	5	6
Formula	C ₁₄₉ H ₁₇₃ La ₃ F ₅₄ N ₁₈ O ₃₀	C ₁₄₉ H ₁₇₃ Eu ₃ F ₅₄ N ₁₈ O ₃₀	C ₁₄₉ H ₁₇₃ Gd ₃ F ₅₄ N ₁₈ O ₃₀	C ₁₃₅ H ₁₄₁ Tb ₃ F ₅₄ N ₁₈ O ₃₀	C ₄₅ H ₄₇ Dy F ₁₈ N ₆ O ₁₀	C ₁₄₉ H ₁₇₃ Er ₃ F ₅₄ N ₁₈ O ₃₀
<i>F</i> _w	4138.78	4177.93	4193.80	3998.42	1336.39	4223.83
Crystal system	Monoclinic	Monoclinic	Monoclinic	Monoclinic	Monoclinic	Monoclinic
Space group	<i>C2/c</i>	<i>C2/c</i>	<i>C2/c</i>	<i>C2/c</i>	<i>P2₁/n</i>	<i>C2/c</i>
<i>a</i> (Å)	50.575(6)	50.142(5)	49.926(3)	49.914(19)	12.6610(12)	49.977(11)
<i>b</i> (Å)	12.6932(12)	12.6433(12)	12.6037(5)	12.461(4)	17.3720(15)	12.631(3)
<i>c</i> (Å)	28.871(3)	28.692(2)	28.6405(16)	28.558(10)	24.491(2)	28.671(6)
α (°)	90	90	90	90	90	90
β (°)	100.922(3)	101.271(3)	101.279(3)	101.821(8)	93.967(6)	101.550(10)
γ (°)	90	90	90	90	90	90
<i>V</i> (Å ³)	18 298(3)	17 389(3)	17 674.0(16)	17 386(11)	5373.8(8)	17 733(7)
<i>Z</i>	4	4	4	4	4	4
<i>D</i> _{calcd} (Mg m ⁻³)	1.511	1.566	1.576	1.528	1.652	1.582
μ (mm ⁻¹)	0.816	1.169	1.241	1.333	8.547	1.535
<i>F</i> (0 0 0)	8360	8432	8444	7992	2668	8492
Crystal size (mm ³)	0.26 × 0.24 × 0.22	0.24 × 0.22 × 0.22	0.26 × 0.24 × 0.22	0.22 × 0.20 × 0.18	0.20 × 0.18 × 0.14	0.20 × 0.18 × 0.12
θ range for data collection (°)	1.84–25.02	1.45–25.02	1.45–25.02	1.46–25.02	3.12–72.72	1.45–25.02
Reflections collected/unique	68 912/15 954	68 008/15 737	70 381/15 574	59 484/15 238	42 338/10 500	68 448/15 647
<i>R</i> _(int)	0.0786	0.0381	0.0423	0.0540	0.0807	0.0360
Data/restraints/parameters	15 954/295/1244	15 737/295/1244	15 574/295/1244	15 238/228/1183	10 500/57/762	15 647/474/1370
GOF on <i>F</i> ²	1.143	1.118	1.059	1.045	1.080	1.072
<i>R</i> ₁ [<i>I</i> > 2 σ (<i>I</i>)]	0.0468	0.0388	0.0320	0.0433	0.0587	0.0504
<i>wR</i> ₂ [<i>I</i> > 2 σ (<i>I</i>)]	0.1155	0.0887	0.0784	0.1110	0.1498	0.1169
<i>R</i> ₁ (all data)	0.0508	0.0407	0.0346	0.0511	0.0685	0.0524
<i>wR</i> ₂ (all data)	0.1180	0.0898	0.0800	0.1164	0.1682	0.1182

Fig. 1. In complex 3, the Gd(III) ion is eight-coordinated in slightly distorted dodecahedron geometry. Two oxygen atoms of the N–O groups from nitronyl nitroxide radicals and six oxygen atoms from three different hfac anions are coordinated to the metal ions. The bond lengths of Gd(1)–O(radical) are Gd(1)–O(1) 2.3328(20) Å and Gd(1)–O(3) 2.3412(18) Å, while the bond lengths of Gd(1)–O(hfac) are in the range of 2.3481(22)–2.4155(20) Å. These bond lengths are comparable to the reported lanthanide–nitronyl nitroxide complexes.¹⁶ The angles between the N–O groups from two radical ligands and Gd(III) ion

are: N(1)–O(1)–Gd(1) 137.429(16)°, N(4)–O(3)–Gd(1) 138.962(16)° and O(1)–Gd(1)–O(3) 139.416(68)°. The nitronyl nitroxide moiety O1–N1–C1–N2–O2 makes a dihedral angle of 2.020(24)° with the plane of benzene ring.

In complex 3, the intermolecular hydrogen bonds occur between one carbon atom from one radical group and one fluorine atom from another hfac ion group (3.364 Å, C(6)–H6A...F(16)). This kind of alternate hydrogen bonds form 1D chain structure in complex 3, which is demonstrated in Fig. 2.

The structure of the complexes 1, 2, 4, 5 and 6 are similar to complex 3, except for the substitution of Gd(III) with La(III), Eu(III), Tb(III), Dy(III) and Er(III) ions, which makes the bond distances and angles vary a little (Table S1†). In complex 1, the nitronyl nitroxide moiety O1–N1–C1–N2–O2 makes a dihedral angle of 1.556(27)° with the plane of benzene ring, while in complex 2 is 1.861(35)°, complex 4 is 2.493(37)°, complex 5 is 4.061(43)° and complex 6 is 3.212(57)°. The structure of complexes 1, 2, 4, 5 and 6 is shown in Fig. S1–S5 (ESI†).

The shape measure

There are many kinds of coordination geometries in eight-coordinated complexes. Three high-symmetry polyhedra are used as a method of analysis of the shape. They are: the trigonal dodecahedron (*D*_{2d}-DD), the bicapped trigonal prism (*C*_{2v}-TP), and the square antiprism (*D*_{4d}-AP) respectively.¹⁷ There exists an intrinsic relationship between the dihedral angles (one for each

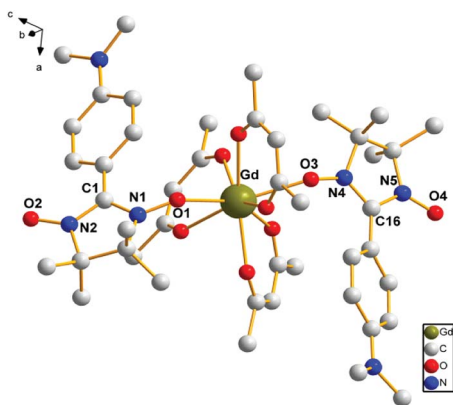


Fig. 1 The crystal structure of complex 3. Fluorine and hydrogen atoms are not shown for the sake of clarity.



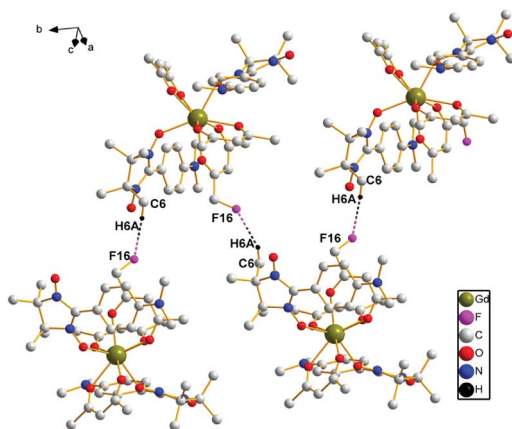


Fig. 2 A sketch of the intermolecular hydrogen bonds of complex 3.

Table 2 *S* values of shape-measure calculations for complexes 1–6

Ln(III)	<i>S</i> (<i>D</i> _{2d})	<i>S</i> (<i>C</i> _{2v})	<i>S</i> (<i>D</i> _{4d})
La (1)	6.08	12.06	9.73
Eu (2)	5.15	12.65	10.24
Gd (3)	4.95	12.62	10.43
Tb (4)	9.58	11.77	10.06
Dy (5)	5.51	20.98	18.52
Er (6)	4.83	20.53	10.58

pair of adjacent triangular planes) and the notion of shape, *i.e.*, the symmetry. Therefore, the geometry of complexes was analyzed by comparing all observed dihedral angles in a given structure and the corresponding ideal values.

Based on the crystal data, we carried out the calculations of the shape factor *S* to estimate the degree of distortion of the coordination structure in first coordination sphere. The *S* value is the minimal variance of dihedral angles along all edges given by eqn (1):

$$S(\delta, \theta) = \min \sqrt{\frac{1}{m} \sum_{i=1}^m (\delta_i - \theta_i)^2}, \quad (1)$$

in which *m* is the number of possible edges (*m* = 18 in this study), δ_i and θ_i are the dihedral angle between planes along the *i*th edge, in particular, the value of δ_i is measured in a given structure and the value of θ_i is observed in an ideal structure respectively. The observed dihedral angle between planes along the *i*th edge (θ_i), the dihedral angle for the ideal structure (δ_i) and the estimated *S* values of complexes 1–6 are listed in Tables S2–S7 (ESI†).

The following *S* values of shape measures calculations are shown in Table 2. By comparing the value of *S*, the coordination environments of complexes 1–6 are all distorted dodecahedron.

Powder X-ray diffraction and TG analyses

To confirm whether the crystal structures are truly representative of the bulk materials, the X-ray powder diffraction patterns

(PXRD) of complexes 1–6 have been recorded which are shown in Fig. S6–S8 (ESI†). These patterns indicate that the PXRD patterns are in good agreement with the results simulated from the single crystal data, indicating the purity of the bulk-synthesized materials.

In order to investigate the thermal stability of complexes 1–6, the thermogravimetry-differential thermal analysis (TG-DTA) was studied, and the TG-DTA curve is depicted in Fig. S9–S11 (ESI†). The TG-DTA curves of 1–6 were similar. Herein, complex 1 as a representative example is selected to describe the thermal stability in details. For complex 1, the first stage takes place from 25.00 to 150 °C (the peak of DTA at 150.83 °C) with the weight loss of 11%, corresponding to losing solvent molecules. The second stage takes place from 150 to 500 °C (the peak of DTA at 302.35 °C) with the weight loss of 70%, corresponding to the skeleton of compound begins collapsed, implying the decomposition of hfac and (NITPh-*p*-N(CH₃)₂)₂.

Luminescence properties

The luminescent measurements of complexes 2 and 4 were investigated at room temperature in ethanol solution. The results reveal that these compounds exhibit the characteristic emission peaks. For complex 2 (Fig. 3, top), the excitation wavelength for emission spectra is 325 nm. The emission spectra are composed of four main bands at 591 nm (⁵D₀ → ⁷F₁), 614 nm (⁵D₀ → ⁷F₂), 650 nm (⁵D₀ → ⁷F₃), and 700 nm (⁵D₀ → ⁷F₄). The electric dipole transitions emission peak at 614 nm (⁵D₀ → ⁷F₂) is clearly stronger than the magnetic dipole transitions peak at 591 nm (⁵D₀ → ⁷F₁). The fluorescence spectra show the characteristic emission peaks of europium ions.¹⁸ For complex 4 (Fig. 3, bottom), the excitation

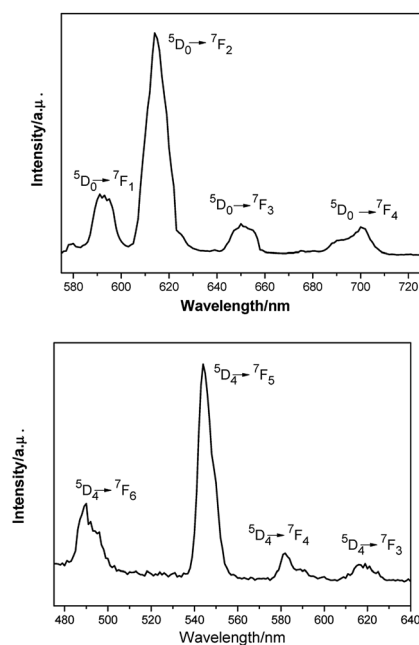


Fig. 3 Room-temperature luminescence spectra of complex 2 ($\lambda_{\text{ex}} = 325$ nm, top) and complex 4 ($\lambda_{\text{ex}} = 290$ nm, bottom) in ethanol solution.



wavelength for emission spectra is 290 nm. The emission peak at 490 nm could be attributed to the $^5D_4 \rightarrow ^7F_6$ transition, and the other three peaks at 544, 582, and 619 nm could be assigned to the $^5D_4 \rightarrow ^7F_5$, $^5D_4 \rightarrow ^7F_4$, and $^5D_4 \rightarrow ^7F_3$ transitions, respectively. Among them, the $^5D_4 \rightarrow ^7F_5$ transition is the strongest. The fluorescence spectra show the characteristic emission peaks of terbium ions.¹⁹

Magnetic properties

Static magnetic properties of 1–6. The temperature dependence of the magnetic susceptibilities of complexes 1–6 were measured for polycrystalline sample in the temperature range 2–300 K under an external magnetic field of 1 kOe. The magnetic behaviors for complexes 1–6 are shown in Fig. 4 and 5.

The room temperature values of $\chi_M T$ are 0.73, 8.64, 12.41, 14.80 and 12.69 $\text{cm}^3 \text{mol}^{-1} \text{K}$ for 1, 3, 4, 5, 6 respectively, in good agreement with the expected values of 0.75, 8.63, 12.23, 14.92 and 12.23 $\text{cm}^3 \text{mol}^{-1} \text{K}$ for one free Ln^{III} ion ($\text{La}^{\text{III}}, ^7F_0$; $\text{Gd}^{\text{III}}, g = 2, ^8S_{7/2}$; $\text{Tb}^{\text{III}}, g = 3/2, ^7F_6$; $\text{Dy}^{\text{III}}, g = 4/3, ^6H_{15/2}$; $\text{Er}^{\text{III}}, g = 6/5, ^4I_{15/2}$) plus two isolated radicals ($g = 2, S = 1/2$).¹⁹ For 2, the $\chi_M T$ value at room temperature is 3.09 $\text{cm}^3 \text{mol}^{-1} \text{K}$ is much higher than the theoretical value of 0.75 $\text{cm}^3 \text{mol}^{-1} \text{K}$ for Eu^{III} ion (7F_0) in the ground state and two organic radicals ($S = 1/2, 0.375 \text{ cm}^3 \text{mol}^{-1} \text{K}$), due to the population of the excited states of Eu^{III} ion at room temperature. Upon cooling, the $\chi_M T$ versus T plots of 1–6 display different behaviors respectively. For complexes 1, 2, 4, 5 and 6, as the temperature is reduced, the $\chi_M T$ value continuously decreases to reach a minimum of

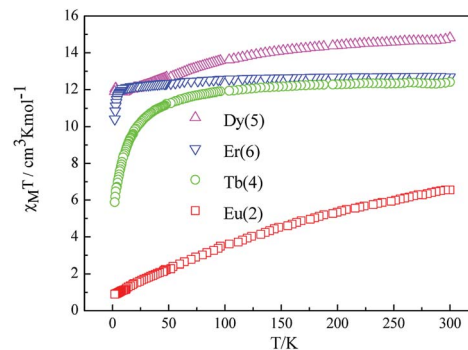


Fig. 5 Temperature dependence of $\chi_M T$ for complexes 2, 4, 5, 6 at 1000 Oe.

0.38 $\text{cm}^3 \text{mol}^{-1} \text{K}$ for 1, 0.419 $\text{cm}^3 \text{mol}^{-1} \text{K}$ for 2, 5.89 $\text{cm}^3 \text{mol}^{-1} \text{K}$ for 4, 10.41 $\text{cm}^3 \text{mol}^{-1} \text{K}$ for 5 and 11.89 $\text{cm}^3 \text{mol}^{-1} \text{K}$ for 6 at $T = 2 \text{ K}$. This probably governed by the depopulation of the Stark sublevels and/or significant antiferromagnetic interaction.

For complex 1, since the $\text{La}(\text{III})$ ion is diamagnetic, the magnetic analysis was thus carried out by using the isotropic spin Hamiltonian $\hat{H} = -2J(\hat{S}_1\hat{S}_2)$ (eqn (2)). Also, intermolecular exchange interaction (zJ') in the molecular field approximation was involved (eqn (3)).

$$\chi'_M = \frac{2Ng^2\beta^2}{KT} \left[\frac{1}{3 + \exp(-2J/KT)} \right] \quad (2)$$

$$\chi_M = \frac{\chi'_M}{1 - (2zJ'/Ng^2\beta^2)\chi'_M} \quad (3)$$

in which J is intramolecular exchange integral between radicals, and zJ' is the intermolecular interaction. The points below 45 K cannot be reproduced well with this model. The best fitting above 45 K gives $g = 2.01, J = -8.2 \text{ cm}^{-1}$ and $zJ' = 1.1 \text{ cm}^{-1}$. The negative value of J indicates the antiferromagnetic interaction between nitronyl nitroxide radicals. Moreover, the little positive of zJ' shows the very weak ferromagnetic interaction between two adjacent molecules. The plot of χ_M^{-1} vs. T obeys the Curie–

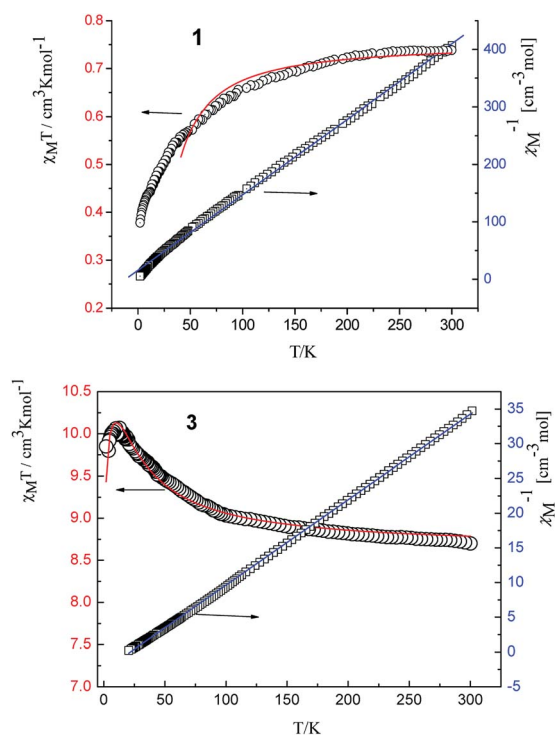


Fig. 4 Temperature dependence of $\chi_M T$ (O) and plot of χ_M^{-1} vs. T of complexes 1 and 3. The solid lines represent the theoretical values based on the corresponding equations.

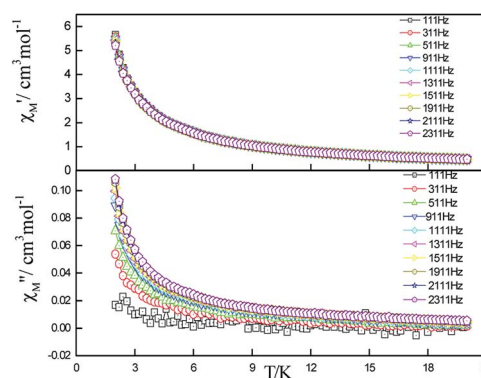


Fig. 6 Frequency dependence of in-phase (top) and out-of-phase (down) components of the ac magnetic susceptibility for 5 under zero applied dc field.



Weiss law between 300 and 2 K, and yields $C = 0.756 \text{ cm}^3 \text{ mol}^{-1} \text{ K}$ with $\theta = -12.8 \text{ K}$. The negative value of θ further confirms the existence of antiferromagnetic coupling between spin carriers.

For complex 3, with the temperature decreases, the $\chi_M T$ value gradually increases to a maximum of $10.03 \text{ cm}^3 \text{ mol}^{-1} \text{ K}$ at 7.97 K, indicating the existence of ferromagnetic coupling between Gd(III) ion and nitronyl nitroxide. Below 7.97 K, $\chi_M T$ decreases quickly to $9.84 \text{ cm}^3 \text{ mol}^{-1} \text{ K}$ at 1.99 K. Based on the isotropic Hamiltonian $\hat{H} = -J_1(\hat{S}_{\text{Gd}} \times \hat{S}_{\text{rad1}} + \hat{S}_{\text{Gd}} \times \hat{S}_{\text{rad2}}) - J_2 \hat{S}_{\text{rad1}} \times \hat{S}_{\text{rad2}}$, eqn (4) is introduced to analyze the magnetic coupling strength, where J_1 and J_2 represent the magnetic coupling for the Gd–radical and radical–radical, respectively.

$$\chi_M = \frac{Ng^2\beta^2}{6KT} \frac{105 + 479 \exp\left(\frac{16J_1}{KT}\right) + 252 \exp\left(\frac{7J_1}{KT}\right) + 252 \exp\left(\frac{9J_1 - 2J_2}{KT}\right)}{6 + 10 \exp\left(\frac{16J_1}{KT}\right) + 8 \exp\left(\frac{7J_1}{KT}\right) + 8 \exp\left(\frac{9J_1 - 2J_2}{KT}\right)} \quad (4)$$

The best fitting results give $J_1 = 2.0 \text{ cm}^{-1}$, $J_2 = -7.8 \text{ cm}^{-1}$ and $g = 2.00$, which is in the range for other similar Gd–radical compounds.¹⁶ The positive value of J_1 shows the ferromagnetic coupling between the Gd(III) ion and nitronyl nitroxide radical, while the negative J_2 indicates the next nearest-neighbor (NNN) antiferromagnetic coupling between the intramolecular radicals. The plot of χ_M^{-1} vs. T obeys the Curie–Weiss law $1/\chi_M = (T - \theta)/C$ between 300 and 2 K, and yields $C = 8.8 \text{ cm}^3 \text{ mol}^{-1} \text{ K}$ with $\theta = 3.2 \text{ K}$. The positive value of θ further confirms the existence of ferromagnetic coupling between spin carriers. The magnetization data of the field dependent magnetization at 2.0 K (Fig. S12†) climbs up quickly until 10 kOe, and then rises up gradually to 70 kOe with an effective moment of $8.38 \mu_B$, which is in smaller than the expected value of $S = 9/2$ under ferromagnetic interaction per GdRad₂ unit ($9.00 \mu_B$), indicating significant spin frustration behaviour because of the competing exchange interactions between J_1 and J_2 .

Dynamic magnetic properties of 4 and 5. To study the slow relaxation of the magnetization of compounds 4 and 5, ac

magnetic susceptibility studies were performed in a zero applied dc field, which were oscillating at frequencies in the range 111–2311 Hz. For complexes 4 and 5, no peaks of frequency-dependent in-phase signals (χ') were observed (Fig. 6 for 5 and Fig. S13 for 4 in the ESI†), moreover, the out-of-phase susceptibilities (χ'') clearly display frequency-dependent signals, which indicate the presence of slow magnetic relaxation in complexes 4 and 5.²⁰ No peaks of frequency-dependent out-of-phase signals (χ'') were observed, which revealed that the quantum tunneling mechanical (QTM) process in 4 and 5 are pronounced. In order to reduce the QTM effect, the variable-temperature ac susceptibilities were determined again under a dc field of 2000 Oe (Fig. 7 for 5 and Fig. S14 for 4 in the ESI†). For 5, good peak shapes in both in-phase (χ') and out-of-phase

(χ'') curve were evidently observed; these phenomena indicate that the QTM effect is basically suppressed in 5 under an external 2000 Oe dc field. However, there are still no maxima peaks in both in-phase and out-of-phase curve for complex 4, which illustrate larger QTM effect in 4.

For complex 5, the Cole–Cole diagrams (Fig. 8), which were measured at temperatures of 2.0, 2.2 and 2.4 K, exhibit a quasi-semicircular shape that can be fitted to the generalized Debye model with α values of 0.34, 0.39 and 0.37, from 2 K to 2.4 K. The parameter φ ($\varphi = (\Delta T_p/T_p)/\Delta(\log f)$) was calculated and a value of 0.36 was obtained, which excludes the possibility of a spin-glass ($0.01 < \varphi < 0.08$).²¹ Plots of $\ln \tau^{-1}$ versus T^{-1} display linear dependence indicating spin reversal by the thermally activated Orbach mechanism process (Fig. 9). The Arrhenius fit ($\tau = \tau_0 \exp(\Delta_{\text{eff}}/k_B T)$) gives the effective energy barrier (Δ_{eff}/k_B) of $(23.44 \pm 1.68) \text{ K}$ and the pre-exponential τ_0 of $(7.15 \pm 0.72) \times 10^{-9} \text{ s}$ ($R = 0.925$) by ac versus T data under a dc field of 2000 Oe, which fall in the range well for SMMs.^{22,23}

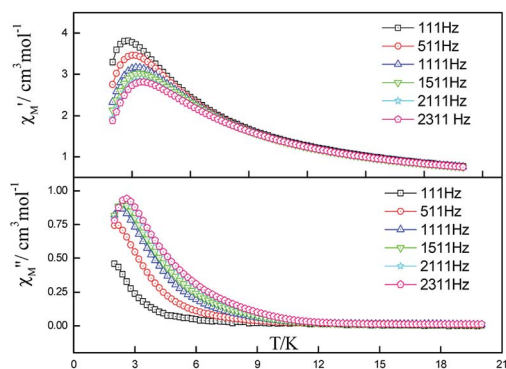


Fig. 7 Frequency dependence of in-phase (top) and out-of-phase components of the ac magnetic susceptibility for 5 under 2000 Oe applied dc field.

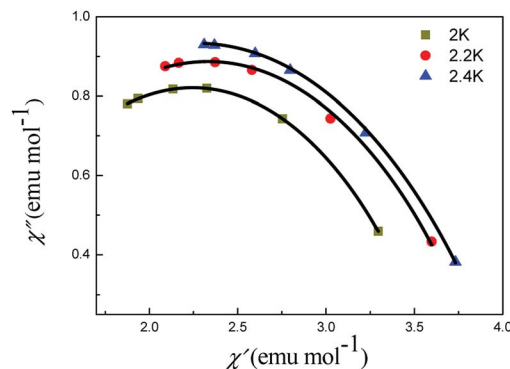


Fig. 8 Cole–Cole plots of 5 under 2000 Oe. The black lines are results of fitting using the Debye model.



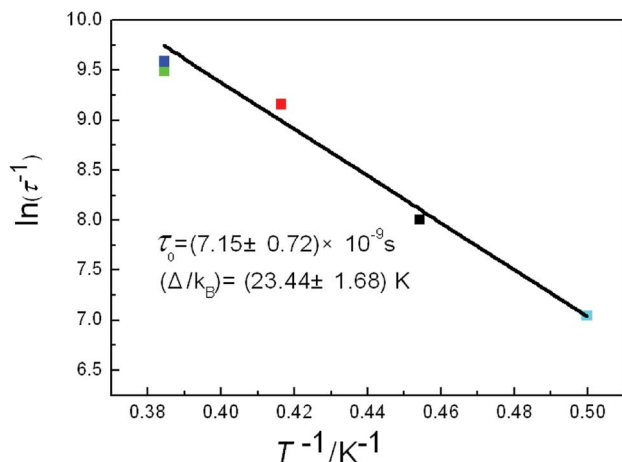


Fig. 9 Plot of $\ln \tau^{-1}$ vs. T^{-1} of 5 under 2000 Oe dc field. The black line is the fitting result using the Arrhenius law.

Conclusions

In summary, six lanthanide coordination complexes have been synthesized and structurally characterized. Dc magnetic studies show that ferromagnetic metal–radical interactions take place in complex 3. Ac magnetic studies for compounds 4 and 5 show clear frequency dependence of the out-of-phase susceptibility. With the application of external field (2000 Oe), good peak shapes of the out-of-phase and in-phase signals were obtained in 5, which give an energy barrier of (23.44 ± 1.68) K. It should be noted that multiple relaxation events can occur for single lanthanide sites. Thus, a more precise result must wait for low temperature measurements ($T < 1.0$ K) by using a micro-SQUID or more AC curves under different magnetic fields.

Acknowledgements

This work was supported by the National Natural Science Foundation of China (No. 21371104, 20771081, 21101096, and 21471084) and MOE Innovation Team (IRT13022) of China.

Notes and references

- D. Gatteschi, R. Sessoli and J. Villain, *Molecular Nanomagnets*, Oxford University Press, 2006.
- (a) R. Sessoli, H.-L. Tsai, A. R. Schake, S. Wang, J. B. Vincent, K. Folting, D. Gatteschi, G. Christou and D. N. Hendrickson, *J. Am. Chem. Soc.*, 1993, **115**, 1804–1806; (b) R. Sessoli, D. Gatteschi, A. Caneschi and M. Novak, *Nature*, 1993, **365**, 141–143; (c) S. M. J. Aubin, M. W. Wemple, D. M. Adams, H.-L. Tsai, G. Christou and D. N. Hendrickson, *J. Am. Chem. Soc.*, 1996, **118**, 7746–7754; (d) S. L. Castro, Z. Sun, C. M. Grant, J. C. Bollinger, D. N. Hendrickson and G. Christou, *J. Am. Chem. Soc.*, 1998, **120**, 2365–2375; (e) H. Oshio, N. Hoshino and T. Ito, *J. Am. Chem. Soc.*, 2000, **122**, 12602–12603.
- (a) A. Caneschi, D. Gatteschi, N. Lalioti, C. Sangregorio, R. Sessoli, G. Venturi, A. Vindigni, A. Rettori, M. G. Pini and M. A. Novak, *Angew. Chem., Int. Ed.*, 2001, **40**, 1760–1763; (b) R. Clérac, H. Miyasaka, M. Yamashita and C. Coulon, *J. Am. Chem. Soc.*, 2002, **124**, 12837–12844; (c) R. Lescouëzec, J. Vaissermann, C. Ruiz-Pérez, F. Lloret, R. Carrasco, M. Julve, M. Verdaguer, Y. Dromzee, D. Gatteschi and W. Wernsdorfer, *Angew. Chem., Int. Ed.*, 2003, **42**, 1483–1486; (d) T.-F. Liu, D. Fu, S. Gao, Y.-Z. Zhang, H.-L. Sun, G. Su and Y.-J. Liu, *J. Am. Chem. Soc.*, 2003, **125**, 13976–13977.
- (a) N. Ishikawa, M. Sugita, T. Ishikawa, S. Koshihara and Y. Kaizu, *J. Am. Chem. Soc.*, 2003, **125**, 8694–8695; (b) R. Sessoli and A. K. Powell, *Coord. Chem. Rev.*, 2009, **253**, 2328–2341; (c) L. Sorace, C. Benelli and D. Gatteschi, *Chem. Soc. Rev.*, 2011, **40**, 3092–3104.
- (a) L. Bogani, C. Sangregorio, R. Sessoli and D. Gatteschi, *Angew. Chem., Int. Ed.*, 2005, **44**, 5817–5821; (b) H.-X. Tian, R.-N. Liu, X.-L. Wang, P.-P. Yang, Z.-X. Li, L.-C. Li and D.-Z. Liao, *Eur. J. Inorg. Chem.*, 2009, 4498–4502; (c) F. Ortu, J. Liu, M. Burton, J. M. Fowler, A. Formanuk, M.-E. Boulon, N. F. Chilton and D. P. Mills, *Inorg. Chem.*, 2017, **56**, 2496–2505.
- (a) G. Poneti, K. Bernot, L. Bogani, A. Caneschi, R. Sessoli, W. Wernsdorfer and D. Gatteschi, *Chem. Commun.*, 2007, 1807–1809; (b) F. Pointillart, K. Bernot, G. Poneti and R. Sessoli, *Inorg. Chem.*, 2012, **51**, 12218–12229; (c) R.-N. Liu, C.-X. Xiong, S.-P. Zhao, J. Wu, Q. Li and D. Fang, *Inorg. Chem. Commun.*, 2012, **22**, 104–107.
- R.-N. Liu, L.-C. Li, X.-L. Wang, P.-P. Yang, C. Wang, D.-Z. Liao and J.-P. Sutter, *Chem. Commun.*, 2010, **46**, 2566–2568.
- S. Das, A. Dey, S. Biswas, E. Colacio and V. Chandrasekhar, *Inorg. Chem.*, 2014, **53**, 3417–3426.
- R.-N. Liu, Y. Ma, P.-P. Yang, X.-Y. Song, G.-F. Xu, J.-K. Tang, L.-C. Li, D.-Z. Liao and S.-P. Yan, *Dalton Trans.*, 2010, **39**, 3321–3325.
- X.-H. Yi, K. Bernot, F. Pointillart, G. Poneti, G. Calvez, C. Daiguebonne, O. Guillou and R. Sessoli, *Chem.–Eur. J.*, 2012, **18**, 11379–11387.
- X.-L. Wang, X. Bao, P.-P. Xu and L. Li, *Eur. J. Inorg. Chem.*, 2011, 3586–3591.
- K. Bernot, L. Bogani, A. Caneschi, D. Gatteschi and R. Sessoli, *J. Am. Chem. Soc.*, 2006, **128**, 7947–7956.
- (a) P. Hu, M. Zhu, X.-L. Mei, H.-X. Tian, Y. Ma, L.-C. Li and D.-Z. Liao, *Dalton Trans.*, 2012, **41**, 14651–14656; (b) E. F. Ullman, J. H. Osiecki, D. G. B. Boocock and R. Darcy, *J. Am. Chem. Soc.*, 1972, **94**, 7049–7059.
- (a) *Theory and Applications of Molecular Paramagnetism*, ed. E. A. Boudreaux and L. N. Mulay, Wiley-Interscience, New York, 1976; (b) G. A. Bain and J. F. Berry, *J. Chem. Educ.*, 2008, **85**, 532–536.
- (a) G. M. Sheldrick, *SHELXS 97*, University of Göttingen, Göttingen, Germany, 1997; (b) G. M. Sheldrick, *SHELXL 97*, University of Göttingen, Göttingen, Germany, 1997.
- (a) M.-Y. Song, Y.-F. Hou, L.-M. Wen, S.-P. Wang, S.-T. Yang, J.-J. Zhang, L.-N. Geng and S.-K. Shi, *J. Mol. Struct.*, 2016, **1107**, 174–181; (b) P. Hu, H.-F. Guo, Y. Li and F.-P. Xiao, *Inorg. Chem. Commun.*, 2015, **59**, 91–94; (c) M.-Y. Song, L.-M. Wen, S.-P. Wang, S.-T. Yang, J.-J. Zhang, L.-N. Geng



- and S.-K. Shi, *Inorg. Chim. Acta*, 2015, **430**, 1–7; (d) X.-L. Wang, *Inorg. Chim. Acta*, 2012, **387**, 20–24.
- 17 (a) J. L. Hoard and J. V. Silverton, *Inorg. Chem.*, 1963, **2**, 235–242; (b) S. J. Lippard and B. J. Russ, *Inorg. Chem.*, 1968, **7**, 1686–1688; (c) V. V. Fomenko, L. I. Kopaneva, M. A. Porai-Koshits and T. N. Polynova, *J. Struct. Chem.*, 1974, **15**, 244–249; (d) D. L. Kepert, *Prog. Inorg. Chem.*, 1978, **24**, 179–183.
- 18 (a) S. Swavey and R. Swavey, *Coord. Chem. Rev.*, 2009, **253**, 2627–2638; (b) Z. Ahmed and K. Iftikhar, *Inorg. Chim. Acta*, 2012, **392**, 165–176; (c) P. Coppo, M. Duati, V. N. Kozhevnikov, J. W. Hofstraat and L. De Cola, *Angew. Chem.*, 2005, **117**, 1840–1844; (d) Y. Lu and B. Yan, *J. Mater. Chem. C*, 2014, **2**, 7411–7416.
- 19 (a) Y.-L. Wang, Y.-Y. Gao, Y. Ma, Q.-L. Wang, L.-C. Li and D.-Z. Liao, *J. Solid State Chem.*, 2013, **202**, 276–281; (b) C. Lescop, G. Bussière, R. Beaulac, H. Bélisle, E. Belorizky, P. Rey, C. Reber and D. Luneau, *J. Phys. Chem. Solids*, 2004, **65**, 773–779.
- 20 D. Visinescu, A. M. Madalan, M. Andruh, C. Duhayon, J.-P. Sutter, L. Ungur, W. V. Heuvel and L. F. Chibotaru, *Chem.–Eur. J.*, 2009, **15**, 11808–11814.
- 21 J. A. Mydosh, *Spin glasses: an experimental introduction*, Taylor & Francis, London, 1993.
- 22 (a) L. Bogani, C. Sangregorio, R. Sessoli and D. Gatteschi, *Angew. Chem., Int. Ed.*, 2005, **117**, 5967–5971; (b) K. Bernot, L. Bogani, R. Sessoli and D. Gatteschi, *Inorg. Chim. Acta*, 2007, **360**, 3807–3812.
- 23 (a) R.-N. Liu, C.-M. Zhang, X.-L. Mei, P. Hu, H.-X. Tian, L.-C. Li, D.-Z. Liao and J.-P. Sutter, *New J. Chem.*, 2012, **36**, 2088–2093; (b) H.-X. Tian, X.-F. Wang, X.-L. Mei, R.-N. Liu, M. Zhu, C.-M. Zhang, Y. Ma, L.-C. Li and D.-Z. Liao, *Eur. J. Inorg. Chem.*, 2013, **2013**, 1320–1325; (c) P. Hu, X.-F. Wang, Y. Ma, Q.-L. Wang, L.-C. Li and D.-Z. Liao, *Dalton Trans.*, 2014, **43**, 2234–2243.

